Post-Print of an Accepted Manuscript on the Laboratory of Turbulent Flows Website

The Accepted Manuscript begins on the next page.

Light-scattering of tracer particles for liquid flow measurements

Prashant Das & Sina Ghaemi

Department of Mechanical Engineering, University of Alberta, Edmonton, Canada

E-mail: `ghaemi@ualberta.ca`

Abstract. A variety of modern flow measurement techniques use tracer particles that should accurately follow fluid motions and should scatter sufficient light to be detectable by imagining systems. These two requirements are at odds if they are to be full-filled by varying the tracer size. For this reason, other particle properties such as material, structure, and coating are also considered. While the effect of these properties on the particle response time can be estimated, it is challenging to quantify their effect on the scattered light using the Mie scattering theory. To address this issue, we investigated the light scattering properties of several commercially available tracer particles and provided simple guidelines for selecting appropriate particles. The investigations were carried out using particle images recorded in forward, side, and backward-scatter angles that are typically used in three-dimensional particle tracking velocimetry (3D-PTV). The selected particles represent a wide spectrum of particle sizes and included glass, polymer, and fluorescent particles used in liquid flows. Other properties such as hollow structures and metallic coatings were also investigated. The results showed that glass particles had greater light scattering in the forward-scatter direction, while the polystyrene particles scattered more light in the back-scatter direction. The fluorescent particles had a relatively narrow intensity distribution with a strong side-scatter. We found that silver-coated glass particles had two to four times higher image intensity in the side and back-scatter cameras when compared with uncoated glass particles. The hollow glass particles had a higher forward-scatter compared with the solid glass particles. The recorded images were also used to obtain 3D particle tracks. A large intensity variation was observed along the 3D tracks that was mainly associated with the discretization of particle images on the camera sensor.

1. Introduction

The choice of tracer particle is an important parameter in conducting particle-based velocimetry techniques. An ideal tracer particle is typically defined as one which would faithfully follow the flow. This criterion is quantified by estimating the Stokes number (Stk), which is the ratio of particle response time to a desired time scale of the flow. Parameters like size and density of the particle are then chosen such that the Stokes number falls well below unity ($Stk \ll 1$), thereby ensuring that the particles follow the flow. However, in addition to the particle response time, the light scattering property of the tracer particles is important to ensure that the tracer is detectable by the sensors, and a large signal-to-noise ratio (SNR) is obtained for accurate detection and tracking of the tracer particles [1]. Although theoretically a more powerful laser can increase SNR, this is not always feasible in practice.

The energy of the light-source can be a limiting factor in volumetric measurements using either tomographic particle image velocimetry (Tomo-PIV) or 3D particle tracking velocimetry (3D-PTV) [2, 3]. The volumetric measurements, as opposed to planar PIV, require the laser beam to be expanded into a volume, and the aperture of the cameras to be reduced for a larger depth-of-focus. This typically requires an order of magnitude greater light-source energy when compared with planar measurements. With increasing interest in time-resolved measurements, the light-source energy becomes even more critical as high-repetition lasers and light-emitting diodes provide a smaller energy per pulse relative to the conventional low-repetition lasers. As a result, a few investigations have implemented methods such as multi-pass amplification of laser light to improve the SNR [4, 5]. Another aspect of volumetric measurements is that the tracers are imaged from different angles with respect to the illumination direction, i.e. forward, side, and back-scattering directions. This also poses a unique challenge since the intensity of scattered light can significantly change with the imaging angle. Therefore, to optimize the use of an illumination source, it is prudent to know the variation in the scattered light intensity of tracers across different imaging angles.

For measurement in air flows, liquid droplets that are approximately 1 μm in diameter (d_p) are commonly used [6]. For large measurement volumes in air, larger tracers such as helium-filled soap bubbles have been used to scatter sufficient light while maintaining a small Stk [7, 8, 9]. For high-speed air flows, there have been a few investigations of small solid tracers with short response time [10, 11]. However,

investigations of tracer particles for liquid flows, and in particular their light scattering properties, are rare.

In liquid flows, the particle-to-fluid density ratio is relatively small - the ratio can even be equal to one for a hollow particle (a spherical shell). Therefore, larger particles, in the order of $d_p = 10$ μm, can be used while maintaining a sufficiently small Stk. The diameter of these particles is larger than the light wavelength ($\lambda < 1$ μm), and the light scattering falls in the Mie regime where the scattering power is proportional to d_p^2 [12]. The scattering power is also proportional to the refractive index ratio $m = n_p/n_f$, where n_p and n_f are the refractive indices of the particle and the fluid medium respectively. Typically, m for solid tracers in water is smaller than 1.2, which results in a smaller scattering intensity relative to liquid droplets in air with larger n_p/n_f ratio.

For homogeneous spheres, the light intensity in the forward-scattering direction is stronger relative to other scattering directions, and is mainly attributed to the diffraction mechanism [13]. Here, homogeneous refers to spheres that are not hollow, nor their surface is coated with a different material. For such spheres, the side and back-scatter intensities depend largely on reflection and refraction, which depend on the sphere's refractive index. Since typical planar experiments have the cameras aligned in a side-scatter configuration, it is desirable to use tracers that have a greater refractive index. This is typically achieved using particles that consist of a hollow spherical shell, or particles that are coated with a thin layer of silver [13]. However, if the hollow shells are broken or the silver coating is not uniform, translation and rotation of these heterogeneous particles may result in temporal variation of the scattered light. Such a geometric heterogeneity, among other mechanisms such as variation in laser intensity and image discretization, can result in de-correlation and track loss in Lagrangian particle tracking algorithms.

For spheres that are coated with metals, like silver for example, the refractive index of their coating is a complex number ($n_p = n_r + in_i$). Here, the imaginary component represents the attenuation of light waves due to Joule heating, which in the case of metals is large [13, 14]. However, the reflectivity R, which is related to refractive index as $R = \frac{(1-n_r)^2 + n_i^2}{(1+n_r)^2 + n_i^2}$, is also large for metals due to a large n_i. For example, silver, which has a refractive index of $n_p = 0.05 + 3.38i$ [15], has a high reflectivity of $R = 0.98$, as opposed to polystyrene ($n_p = 1.59$) which has a reflectivity of $R = 0.05$. Since the side-scatter and back-scatter primarily depend on reflectivity and refraction, particles with a metallic coating are expected to scatter more light in these directions.

A polar plot of scattered light intensity as a function of viewing angle based on Mie scattering [14, 16] of homogeneous polystyrene and silver spheres in water is shown in Figure 1. Note that the radial axis here is plotted on a log scale. For both cases the sphere diameter is 10 μm and the wavelength of incident light is 527 nm. It is observed that the scatter intensity varies significantly with viewing angle for the polystyrene sphere. The high forward-scatter in this case is confined to a narrow zone near $\theta = 0°$ while the side-scatter ($\theta = 90°$) is comparatively lower. For the silver particle, we note a more even distribution of intensity with the viewing angle, with the side and back-scatter being of similar order. We note that the silver spheres have higher side and back-scatter intensities relative to the polystyrene particles. Therefore, heterogeneous tracers like hollow glass spheres with metallic coating are expected to provide a stronger side and back-scatter intensities due to their high reflectivity [13, 17], with hollow structure being also useful in reducing their density.
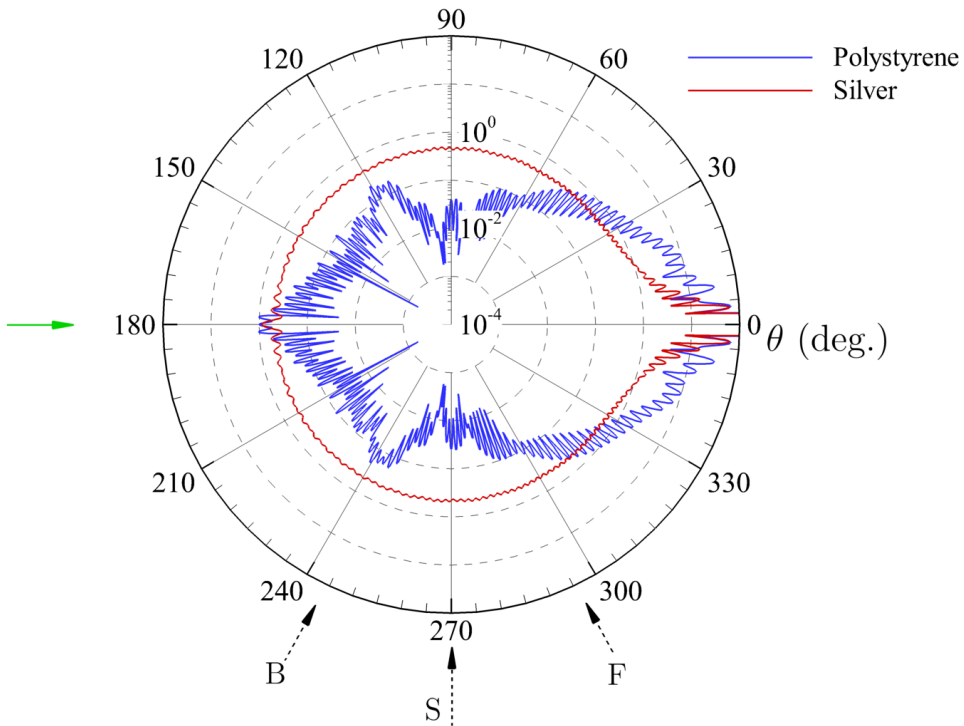

Figure 1: Mie scatter intensity as a function of the viewing angle in polar coordinates [16]. The radial axis is in log scale. The refractive indices of the two 10 μm particles shown are, $n_p = 1.59$ for polystyrene, and $n_p = 0.05+3.38i$ for silver. The solid green arrow on the left shows the direction of incident light, which has a wavelength of 527 nm. The dotted black arrows show the forward (F), side (S) and back-scatter (B) viewing angles studied in the present experiments, and are described later in section 2.2.

In addition to polymers, glass, and metal-coated particles, fluorescent particles are also used for specific measurements. They are commonly used in experiments which require isolating the tracers from other light scattering interfaces like walls in boundary layer measurements [18], or bubbles in multi-phase flows [19]. These tracers are typically hollow shells doped with a fluorescent dye and their scattered intensity is proportional to dye volume. Fluorescence is typically isotropic, which means that the scattered light due to the fluorescence process does not depend on the viewing angle [17]. In summary, properties such as material, structure, and coating should be carefully chosen to improve the light-scattering properties of tracer particles.

The present work evaluates the light scattering properties of several commercially available tracers for liquid flows. The size of the tracers varies from 2 μm - 80 μm and the tracers include particles with different material (glass/polymer/fluorescence dye), structure (hollow/filled spheres), and with metallic coating. To address the issues relevant to volumetric measurements, we investigate the light intensity for different imaging angles used in a 3D-PTV measurement. The acquired images are also processed using the shake-the-box (STB) algorithm [3] to investigate the fluctuation of light intensity along the reconstructed 3D tracks.

2. Experimental Method

2.1. Tracer particles

The tracer particles used in this study are selected such that they span a range of characteristics. We investigate twelve different tracers which are broadly grouped into three categories of glass, polymer, and fluorescent particles, as shown in Table 1. The table includes particle diameter (d_p), material, particle density (ρ), commercial name and manufacturer for each particle. The nomenclature used for referring to the particles is in the form of XYZ-D, where X is the particle type (G - Glass, P - Polymer, F - Fluorescent), and Y is the particle coating (S - Silver-coated, U - Uncoated). The third letter, Z, indicates if the particle is a homogeneous solid sphere (S), or a hollow shell (H). The letter D represents the mean particle diameter in μm. For glass particles, we have five different particle sizes. As the particle codes in Table 1 indicate, the glass particles include homogeneous solid spheres, hollow spheres, and silver-coated particles. For the polymers, we also have five different particles which include polyamide and polystyrene materials. For fluorescent particles, we have two different sizes.

For particle sizes, either the mean diameter or the particle diameter range as reported by the manufacturer is provided in the table. A few available details of some of the particles studied are presented hereon, along with Scanning Electron Micrsocope (SEM) images of the tracer particles shown in Figure 2. The GSS-2 particles are the smallest particles investigated here, and have a thin silver coating. Their SEM image in Figure 2 show that the GSS-2 particles are relatively poly-disperse, with particles in the range of 0.5 to 3 μm. The image also shows that the silver coating may partially cover the surface, resulting in structural asymmetry. The GUS-7 particles (soda-lime glass) have a mean diameter in the range of 7-10 μm, and their refractive index was $n_p = 1.52$. Their SEM image shows a wide range of particle size, ranging from 1 to 12 μm. In addition, microfibers and non-spherical objects are also present. The GSH-10, GUH-12, and GSH-13 particles are poly-disperse with particles in the rage of 1-20 μm. The silver coating of the GSH-10 and GSH-13 appears uniform. No evidence of broken shells is present in the SEM images. The PUS-5 particles have a D50 of 5 μm and a D90 of approximately 13 μm, and a refractive index of $n_p = 1.51$. The SEM images reveal that these particles are non-spherical. The PUS-10, PUS-20 and PUS-40 particles, which are from the same manufacturer, have a narrow size distribution [20]. The refractive indices of polystyrene and polyethylene particles were $n_p = 1.59$ and 1.55, respectively [21]. According to the manufacturer data, PUS-81 has a diameter range of 75-90 μm, with the mean diameter being approximately 81 μm and the standard deviation being approximately 6 μm. This is consistent with the SEM image of Figure 2. The fluorescent particles FUS-10 and FUS-30 were made from polystyrene and polyethylene shells, respectively. For FUS-10, the excitation and emission wavelength were 530 nm and 607 nm, respectively. FUS-10 particles are mono-disperse as verified by the SEM images. The FUS-30 particles had a mean diameter of approximately 30 μm and a D90 of approximately 40 μm. The particle size range for FUS-30 was 10-45 μm with greater than 90% of the particles being in this size range. They had a peak emission of 607 nm when excited with a laser light at 575 nm wavelength.

2.2. Measurement of scattered light intensity and 3D-PTV

A schematic of the experimental setup used for this work is shown in Figure 3. The field of view (FOV) of the cameras and the coordinate system adopted in this work can be noted from the figure. The setup consisted of a water tank with dimensions of 400 mm $\times$ 150 mm $\times$ 150 mm along the x, y, and z direction, respectively. The

Particle Code	d_p (μm)	Material	ρ (g/cc)	Commercial Name	Manufacturer
GSS-2	2	Glass	4.00	SG02S40 Conduct-O-Fil	Potters
GUS-7	7-10	Soda-lime glass	2.50	Spheriglass® A-Glass 5000	Potters
GSH-10	10	Glass	1.40	S-HGS-10	Dantec Dynamics
GUH-12	12	Borosilicate glass	1.10	110P8	Potters
GSH-13	13	Glass	1.60	SH400S20 Conduct-O-Fil	Potters
PUS-5	5	Polyamide	1.02	Vestosint 2070	Evonik
PUS-10	10	Polystyrene	1.05	Dynoseeds TS-10	Microbeads
PUS-20	20	Polystyrene	1.05	Dynoseeds TS-20	Microbeads
PUS-40	40	Polystyrene	1.05	Dynoseeds TS-40	Microbeads
PUS-81	75-90	Polyethylene	1.25	WPMS-1.25	Cospheric
FUS-10	10	Fluorescent	1.05	PS-FluoRed	microParticles
FUS-30	10-45	Fluorescent	1.09	UVPMS-BR-1.090	Cospheric

Table 1: List of commercial particles and their properties used in the present study. The nomenclature used for each particle is in the form of XYZ-D, where X is the particle type (G - Glass, P - Polymer, F - Fluorescent), Y is the particle coating (S - Silver-coated, U - Uncoated), Z indicates if the particle is Solid (S) or Hollow (H), and D represents the mean particle diameter in μm.

light source was a dual cavity Nd:YLF high-speed laser (Photonics Industries DM20-527-DH) with a wavelength of 527 nm and a maximum pulse energy of 20 mJ per cavity at 1 kHz. Four high-speed CMOS cameras (Phantom V611), with pixel size of 20 μm $\times$ 20 μm and 12-bit resolution (4096 counts) were used. The cameras had a maximum resolution of 1280 $\times$ 800 pixels, and were equipped with 105 mm lenses and Scheimpflug adapters. The aperture size of all cameras were kept at f-number of 16. The laser and the cameras were synchronized using a programmable timing unit (PTU X, LaVision, GmbH). The four cameras were arranged such that camera 1 and 3 collected the forward- and back-scattered light respectively, whereas camera 2 and 4 were in a side-scatter configuration. Camera 2 was nearly perpendicular to the xy plane, whereas cameras 1 and 3 were approximately oriented at 26° relative to the yz plane. Camera 4 was oriented 42° relative to the xz plane.

The imaging field-of-view was 69.9 mm $\times$ 43.7 mm at a digital resolution of 54.6 μm/pixel and magnification of $M = 0.37$. The cameras were approximately 40 cm away from the measurement domain, each imaging through an observation angle of approximately 4°. The Airy disk formed by the diffraction pattern of the particles was approximately 28.4 μm. The geometric image size of the smallest particles (GSS-2) was 0.7 μm while the geometric image size of the largest PUS-81 particles is 29.7 μm. Therefore, the particle image diameter varied from 28.0 to 40.8 μm, which is equivalent

(GSS-2) (GUS-7) (GSH-10)

(GUH-12) (GSH-13) (PUS-5)

(PUS-10) (PUS-20) (PUS-40)
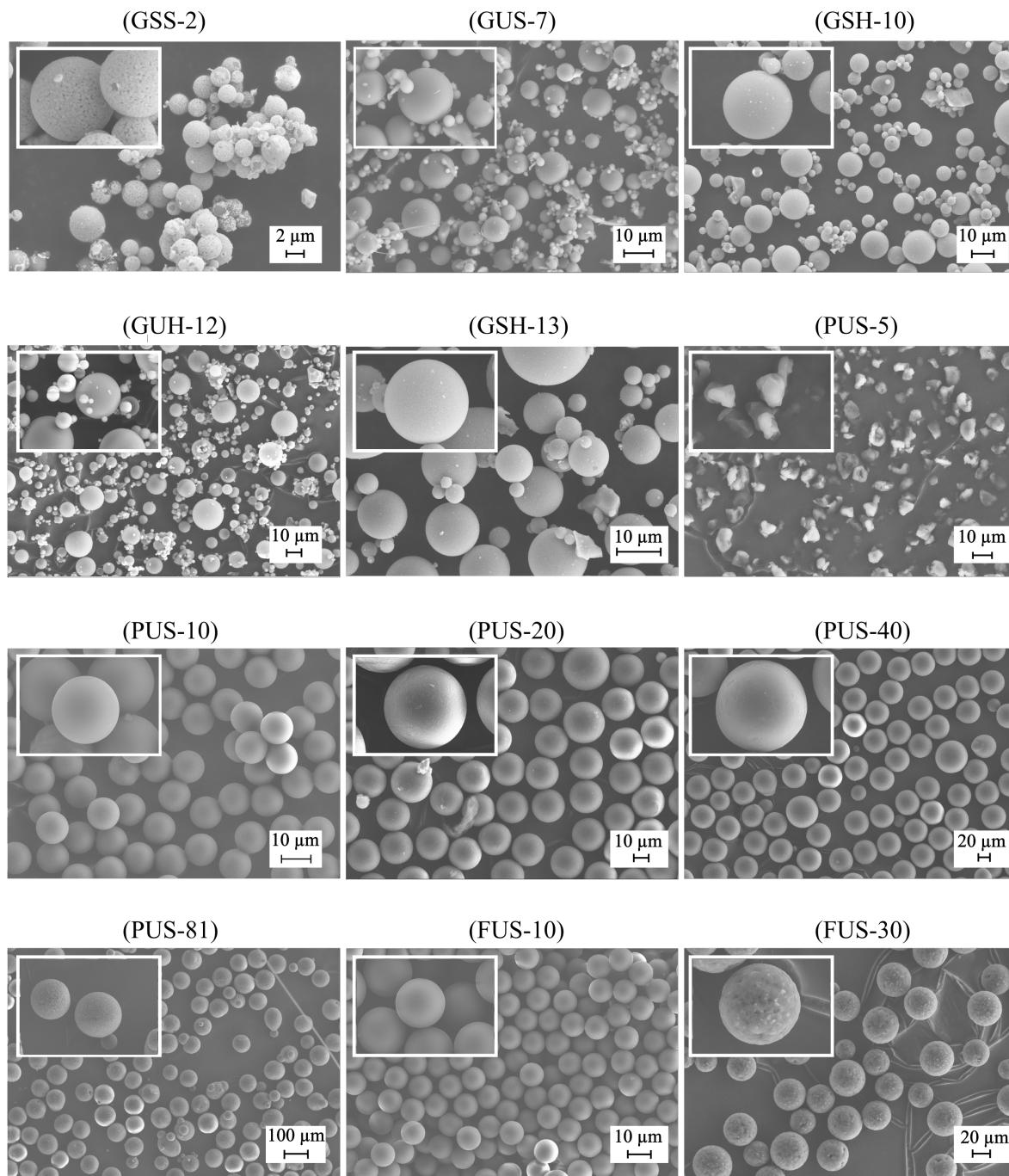
(PUS-81) (FUS-10) (FUS-30)

Figure 2: SEM images of the tracer particles investigated in the present work. The images are labeled using the particle code from Table 1. A scale is included in each image for reference. The inset in each image shows a magnified view of the corresponding particles.

to approximately 2-4 pixel in diameter.

Using a combination of spherical and cylindrical lenses, the laser beam was
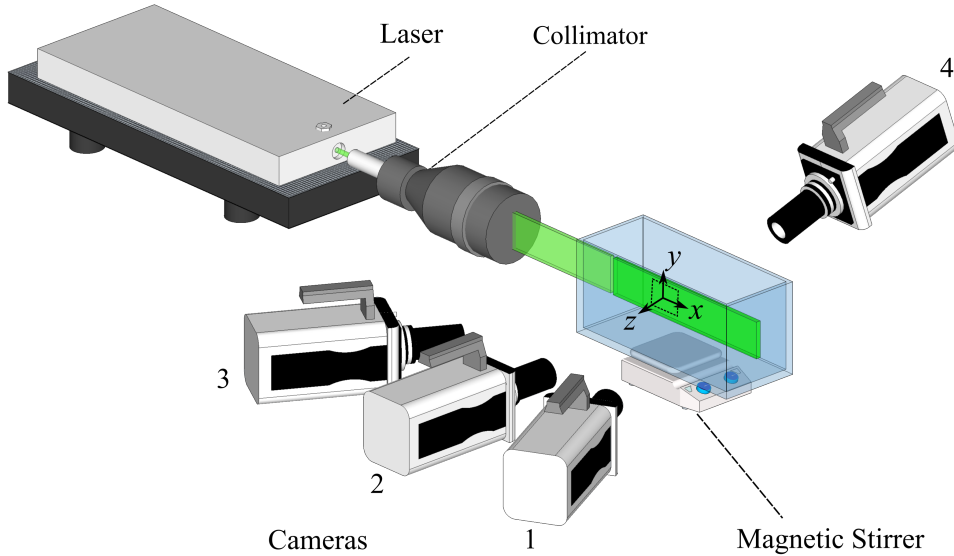
Figure 3: A schematic of the experimental setup used in the present work. The dotted square surrounding the coordinate-system represents the extent of the measured field-of-view (FOV).

collimated into a beam with elliptical cross-section. The major and minor axis of the ellipse were 100 mm and 8 mm, respectively. The elliptical beam was then cropped to form a rectangular cross section with height of 60 mm and thickness of 5 mm in y and z directions, respectively. For imaging the fluorescent particles, band-pass filters which had wavelength limits of [545-800] nm were fitted on the camera lenses.

A magnetic stirrer was used to generate a low speed random flow in the tank with a stirring bar rotating at 100 rpm. For each of the twelve different particles, an estimated quantity was added to the water to result in a particle image density of approximately 0.001 particles per pixel (ppp), equivalent to 70 particles/mm^3. The small ppp minimized obstruction of the camera light-of-sight and increased the continuity of the Lagrangian tracks. For ease of comparison of the light intensity, the laser pulse energy, was kept constant at 11.6 mJ/pulse for 9 out of the 12 particles considered. The laser energy was carefully selected to ensure that only a negligible number of particles saturate the camera (4096 counts) in the strongest light scattering direction. For the 11.6 mJ cases, the PUS-40 tracers had the strongest scattered light with a mean value of 580 counts at the back-scatter direction. For these particles, approximately 3% of the total number of particles had a scatter intensity larger than 4000 counts, i.e. saturating

the 12-bit sensor. The selected laser power allowed to utilize the full dynamic range of the sensor while avoiding clipping the high intensity peaks. The other 3 particles were imaged with different laser energy either due to the particles scattering too little light, or due to the particles being too bright and saturating the camera sensor. For extremely large PUS-81 particles, we had to use a smaller laser power of 1.7 mJ, and for PUS-10 and FUS-10 particles with smaller light scattering we applied 22.2 mJ. The laser power was measured using a laser power meter.

A total of 3000 single-frame images were recorded at a frequency of 500 Hz for each case. This recording frequency resulted in highly resolved tracks with a maximum particle displacement of 1-2 pixel between consecutive images. To compare the scattered intensity of the particles, the particles peak intensities were obtained by detecting the local intensity maxima in the recorded 2D images for each viewing angle. Based on visual inspection of the images, an intensity threshold of 30 counts was used to discard any background noise. A sample of the raw images obtained from the side-scatter camera is presented in Figure 4a and c for PUS-40 and FUS-30 tracers, respectively. Figure 4b and d also show the corresponding enhanced images used for the 3D-PTV processing. For this purpose, the image contrast was first improved by subtracting a sliding minimum over 5 pixels and then normalizing with a local average over 60 pixels. The image enhancement only removes the background noise and does not eliminate any particle image. Note that enhancement is only applied for the 3D-PTV processing and is not used for the assessment of scattered light intensity from 2D images.

The identified particles from the 2D particle-detection algorithm with a threshold of 30 count are marked using red circles in Figure 4c. The intensity threshold is verified here by showing the average image intensity of ten consecutive images in Figure 4e. By comparing this with Figure 4c, we note that the identified particles are present in several images, proving that the weak local-maxima detected in Figure 4c are particles as opposed to background image noise. The two low-intensity particles labeled as 'p1' and 'p2' in Figure 4c have a peak intensity of 39 and 50 counts, respectively. We can note from Figure 4e that these particles can be tracked in time, confirming that the detected intensity maximums are not image noise.

The probability density function (pdf) of the peak intensity of particle images was evaluated for each viewing angle and for each tracer based on the 2D images. A sample pdf is presented in Figure 5 for the three viewing angles of the PUS-40 particles. Due to the presence of a large number of low intensity values, the pdf of peak particle
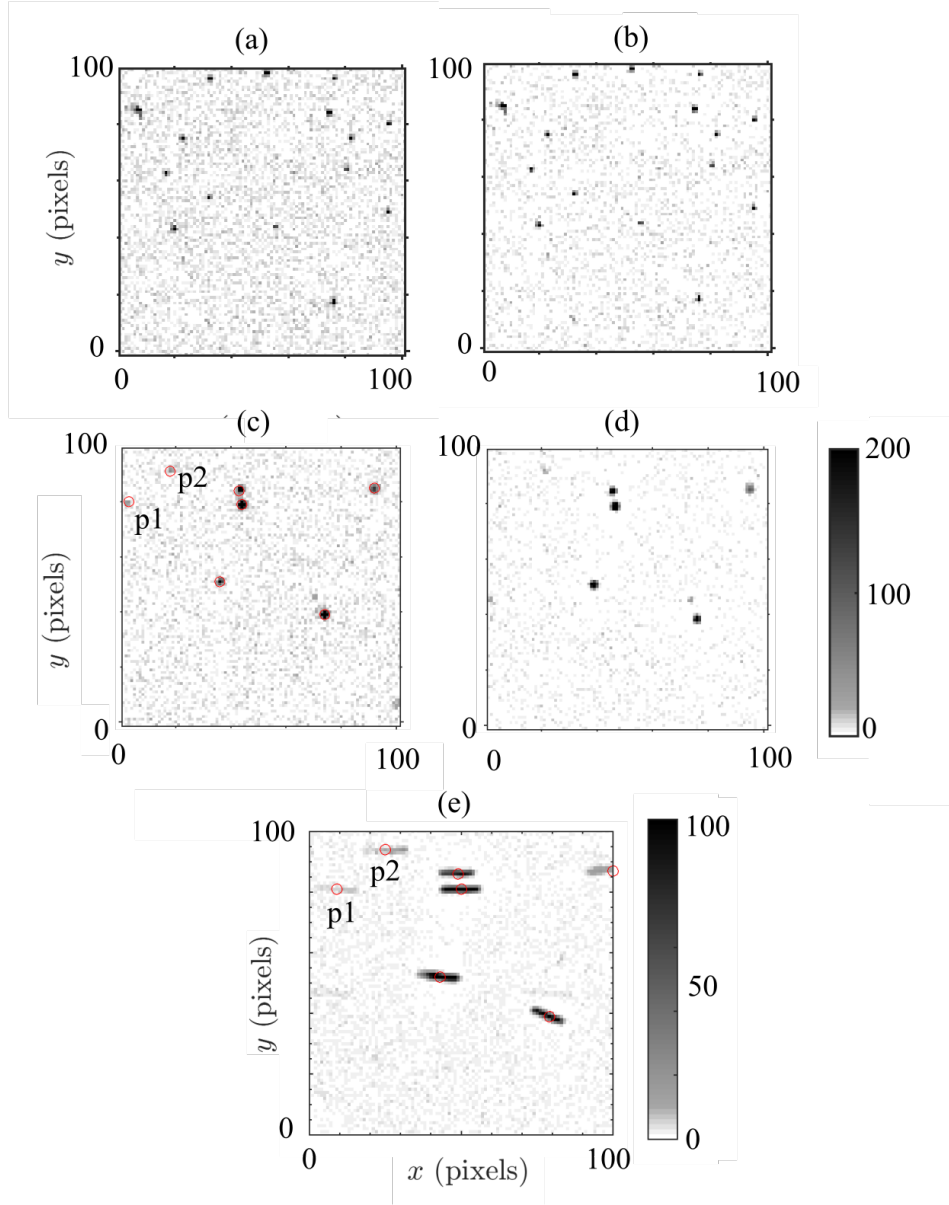
Figure 4: A sample of the raw and enhanced images for PUS-40 (a,b) and FUS-30 (c,d) tracers. (a,c) are the raw images and (b,d) are the enhanced images that are used for 3D-PTV processing. Also superimposed in (d,e) are red circles showing the detected particles based from the raw images. The intensity of the sample particles p1 and p2 labeled in (d) are 39 counts and 50 counts, respectively. (e) The average image intensity for ten consecutive images of FUS-30 tracers.

intensity is non-Gaussian and its maximum is at the smallest intensity. As observed in the SEM images, PUS-40 particles are mono-disperse, and the low intensities can not be due to smaller particles. Our inspection of the time-resolved images suggested that the low-intensity particle images form when the particles cross the boundaries of the
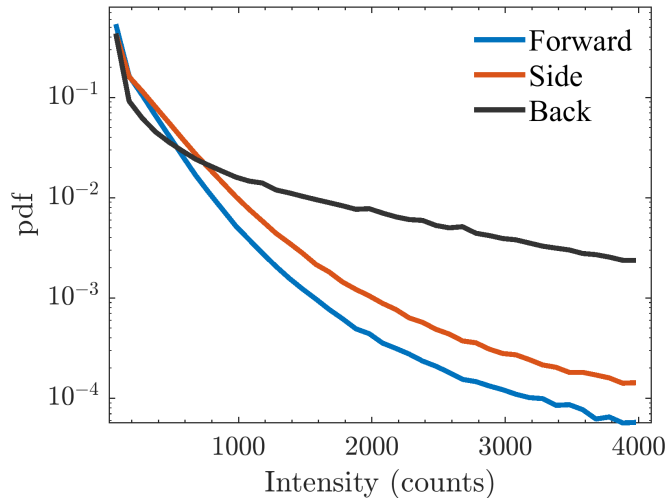
Figure 5: The pdf of particle intensity for forward, side, and back-scatter viewing angles of PUS-40 particles. The mean intensities are 209 counts, 290 counts, and 580 counts for the forward, side and back-scatter viewing angles, respectively.

measurement volume in the out-of-plane direction (z axis). Although we used a knife-edge to obtain a top-hat illumination, the particle images show a transition period with low intensity, over a few time-steps, as they enter (or leave) the illuminated volume. In spite of these low-intensity particles, a comparison across the viewing angles show that a large number of high-intensity particles are found for the back-scatter angle. This also reflects in the mean intensity values, which as noted in the caption of this figure, is higher for the back-scatter relative to the side- and forward-scatter directions. In the following sections, we will present the pdfs for all particle cases in a log-log scale to illustrate the low-intensity portion more clearly. The particle intensity, which is measured in counts, will also be normalized using the corresponding laser power for comparison across all cases. Hence, going forward we shall present the intensity in the unit of counts/mJ.

The image enhancement process and the subsequent 3D-PTV processes were carried out using a commercial software (DaVis 10, LaVision GmbH). The initial mapping function of the imaging system was obtained using a dual-plane target with the two planes separated by 1 mm. To remove the remaining calibration disparities, a volume self calibration process was applied [22]. Next an optical transfer function (OTF) was calculated [23] and used in the STB algorithm to obtain Lagrangian particle tracks [3]. Approximately 450 tracks were found at each time-step. The distribution of laser intensity in the measurement domain was estimated by applying the multiplicative
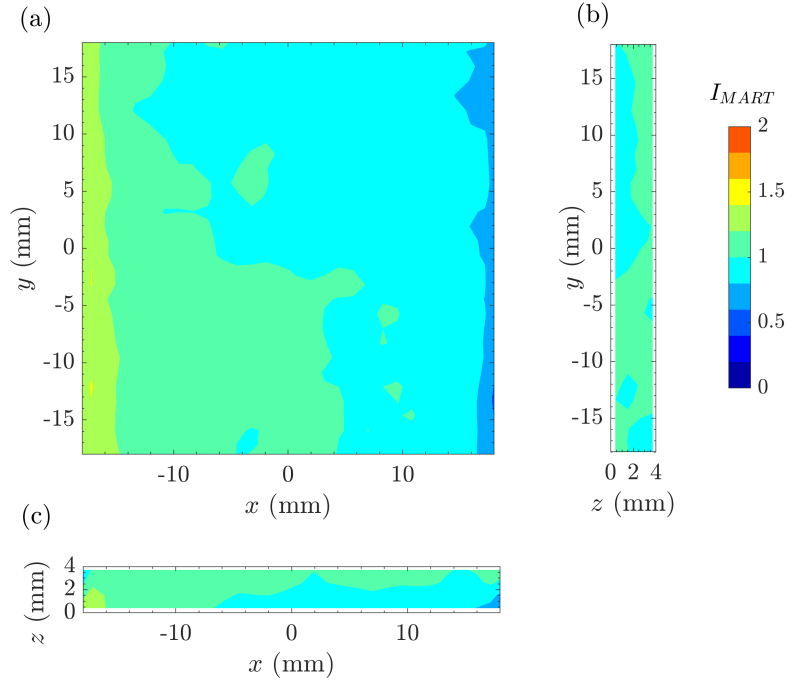
Figure 6: A MART reconstruction of the measurement volume. The contours show the reconstructed light intensity normalized with the mean intensity in the volume. The three planes shown are the (a) xy, (b) yz and (c) zx mid-planes.

algebraic reconstruction technique (MART) to the recorded images [24]. The MART reconstruction was applied to all the data to obtain the average reconstructed intensity, which is normalized by the mean intensity in the volume. The result is presented as I_{MART} in Figure 6. The three planes shown in the figure are the xy, yz and zx mid-planes. It is noted that the maximum variation of intensity in the measurement volume is below 10% of the average intensity. This is associated with the spatial variation of laser power across the illuminated domain.

3. Results

The normalized mean of particle peak intensities (μ_p) and their coefficient of variation (CV) based on the 2D images are presented in Table 2 for different viewing angles. The units of μ_p is counts/mJ, which is obtained by dividing the mean peak intensity (in counts) by the corresponding laser energy (in mJ). CV is evaluated as the percentage ratio of standard deviation of particle peak intensity (σ_p) to the mean of particle peak intensity(μ_p), and can be written as CV $= \frac{\sigma_p}{\mu_p} \times 100$. The table also lists the laser energy

in mJ that is used for each particle case. Additional quantities like CV_i and CV_{tr} that are used to investigate the intensity fluctuations are explained later in section 3.4. The results shown in the table are discussed in the following subsections. In section 3.1 we look at the effect of particle size. Sections 3.2 contains an analysis on the effect of particle material, whereas section 3.3 investigates the effect of particle heterogeneity. In section 3.4, we examine the factors behind the temporal fluctuations of the particle intensity along 3D tracks.

Particle Code	Energy (mJ)	forward-scatter		side-scatter			back-scatter		Tracks
		μ_p	CV(%)	μ_p	CV(%)	CV_i(%)	μ_p	CV(%)	CV_{tr}(%)
GSS-2	11.6	14	160	24	160	4.3	18	160	55
GUS-7	11.6	7	200	6	160	3.3	6	160	72
GSH-10	11.6	19	160	31	160	3.6	23	150	58
GUH-12	11.6	18	180	12	150	3.8	6	150	62
GSH-13	11.6	21	150	35	150	2.7	24	150	70
PUS-5	11.6	14	170	14	170	4.6	8	140	50
PUS-10	22.2	6	180	6	160	5.7	9	120	58
PUS-20	11.6	14	130	13	120	4.5	24	120	61
PUS-40	11.6	18	130	25	120	4.4	50	150	62
PUS-81	01.7	194	150	319	160	6.4	321	150	50
FUS-10	22.2	3	60	5	40	1.3	3	30	47
FUS-30	11.6	28	120	37	140	5.0	24	130	45

Table 2: The mean (μ_p) and coefficient of variation (CV) of particle peak intensity are presented for three viewing angles. CV is evaluated as the ratio of standard deviation (σ) to mean (μ_p) of peak intensity for all the particle detected in the 2D images; $CV = \frac{\sigma_p}{\mu_p} \times 100$. A measure of fluctuation in the laser energy is obtained using the average intensity of particles detected in individual images, which is indicated as μ_i. The ratio of the standard deviation to the mean of μ_i is shown as CV_i, defined as $CV_i = \frac{\sigma_{\mu_i}}{\mu_{\mu_i}} \times 100$. This parameter is only presented for the side-scatter camera. The coefficient of variation of particle intensity along 3D tracks, CV_{tr} is shown in the last column. CV_{tr} is evaluated by first calculating the ratio of standard deviation to mean of the intensity factor, I, along each 3D track. These values are then averaged across all tracks resulting in CV_{tr}. The intensity factor, I, indicates particle intensity along 3D tracks and is calculated based on the iterative particle reconstruction method (IPR) [25] in Davis 10 (LaVision GmbH).

3.1. Effect of size

To investigate the effect of particle size, we consider homogeneous, polymer particles with four different sizes: PUS-5, PUS-10, PUS-20, and PUS-40. PUS-5 is made of polyamide and PUS-10, 20 and 40 are polystyrene particles. Figure 7 shows the normalized mean peak intensity (μ_p) and the probability density function (pdf) of peak intensity for the three viewing angles. The pdf of normalized intensity is presented in Figure 7b for forward-scatter (Camera 1 in Figure 3), in Figure 7c for side-scatter (Camera 2) and in Figure 7d for back-scatter (Camera 3). Camera 4, which is also side-scatter, is omitted for brevity.
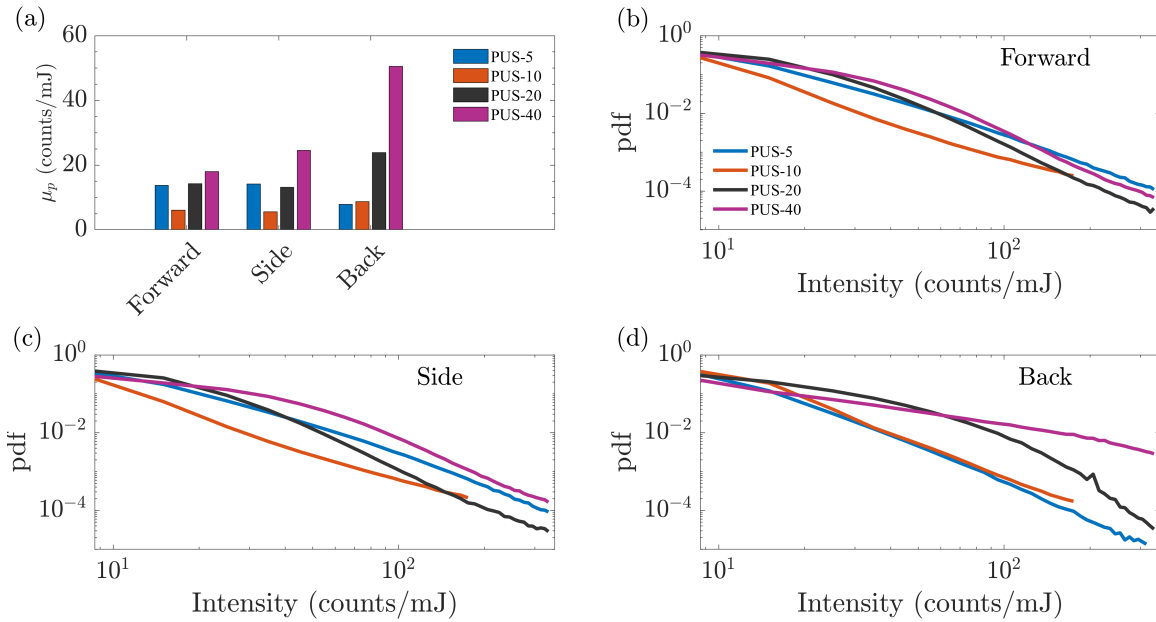

Figure 7: (a) The normalized mean intensity (μ_p) of different polymer particles for the three viewing angles. The pdf of normalized particle intensity for (b) forward-scatter (c) side-scatter and (d) back-scatter viewing angles.

In Figure 7a, the three polystyrene particles have the highest mean intensity in the back-scatter camera, followed by the side-scatter, with the forward-scatter being the weakest. The PUS-5 tracers, which are made of polyamide and are non-spherical, however, have similar mean intensity values in the forward and side-scatter cameras, and lower back-scatter intensity. The forward and side-scatter of PUS-5 are approximately equal to PUS-20. The comparison of PUS-5 with the spherical particles shows that the nonsphericity increases the scattered-light intensity, and makes the forward- and

side-scatter stronger. There is an increase in μ_p with increasing particle size, across all viewing angles. An approximation using a linear fit shows that μ_p is proportional to $0.5d_p$, $0.63d_p$ and $1.24d_p$ in the forward, side, and back-scatter viewing angles, respectively. The increase is therefore most pronounced in back-scatter, with the mean intensity of PUS-40 being approximately 5 times that of PUS-10. It is important to emphasize that the approximate linear increase of scattered intensity with increasing particle diameter is observed here for the peak intensity of the particle images. The scattered intensity, which should be evaluated as the total intensity of the particle image, is expected to be proportional to the cross-sectional area of the particle, i.e. d_p^2.

The above observation regarding the 10 μm polystyrene particles (PUS-10) is consistent with the Mie scatter plot of polystyrene particle in Figure 1 where we note that the back-scatter camera is aligned with a local intensity lobe. In both Figure 1 and PUS-10 results in Figure 7a, back-scatter intensity is slightly larger than the forward and side-scatter intensities, while the forward-scatter is slightly larger than side-scatter. It should be noted that the scatter intensity, as shown in the Mie scatter plot from Figure 1, depends on both the particle size and refractive index [1]. Therefore, the intensity distribution from the Mie scatter of Figure 1 should not be quantitatively compared with the results for the larger PUS-20 and PUS-40 particles in Figure 7a.

In the pdf plots of forward and side-scatter intensities in Figure 7b and c, we note that PUS-40 has the highest and PUS-10 has the lowest pdf for small intensities. For the forward-scatter, the PUS-5 tracers have higher pdf for large intensities. Note that the PUS-5 particles are non-spherical, which could also be a contributing reason for larger pdf values when compared to the spherical PUS-10 particles. In the back-scatter direction shown in Figure 7d, PUS-5 and PUS-10 have approximately the same distribution. PUS-20 and 40 have significantly higher intensity distribution than the PUS-5 and 10 particles in back-scatter. The width of intensity distribution is characterized from the coefficient of variation (CV), which is presented in Table 2. We note that across the PUS-5, 10, 20, 40 particles, the CV in all viewing angles is in the range of 120 - 180 %. The highest CV is observed for PUS-5 and PUS-10 in forward and side-scatter angles. The CV across all viewing angles is smaller for PUS-20 and PUS-40, with the exception of PUS-40 in back-scatter. This observation is in agreement with the intuition that larger mono-disperse particles result in a narrower intensity distribution, whereas poly-disperse particles like PUS-5 (with a D90 of 13 μm) result in a wider intensity distribution.

3.2. Effect of material

To investigate the effect of tracer's material, we start by presenting the intensity distribution of three different particles with approximately similar mean diameter in Figure 8. The particles shown here are made of glass (GUS-7), polystyrene (PUS-10), and polystyrene particles doped with a fluorescence dye (FUS-10). The SEM images showed that GUS-7 is poly-disperse while PUS-10 and FUS-10 are mono-disperse. The refractive indices for the glass and polystyrene tracers are 1.52 and 1.59, respectively. The mean particle image intensities (μ_p) in Figure 8a show that in the forward and side-scatter configuration, GUS-7 has higher intensity when compared to the PUS-10 and FUS-10 particles. In back-scatter direction, PUS-10 particles have the highest μ_p (9 counts/mJ), followed by the glass particles (6 counts/mJ). The fluorescent particles (FUS-10) exhibit higher mean intensity (1.6×) in the side-scatter direction, than in the forward and back-scatter direction. We note from the pdf distributions of Figure 8b-d, that across all viewing angles the fluorescent tracers have the weakest and narrowest intensity distribution, with there being no particles with an intensity larger than 30 counts/mJ. The glass and polystyrene particles (GUS-7 and PUS-10) exhibit approximately similar distributions in the forward and side-scatter directions.

Overall, we note that glass and polystyrene particles have higher μ_p when compared to the fluorescent particles. Between the glass and polystyrene particles, we note that glass particles have larger forward-scatter and polystyrene particles have larger back-scatter intensity. In the side-scatter viewing angle, the difference in μ_p is relatively smaller between glass and polystyrene particles. The coefficient of variation (CV) in Table 2 shows that CV of the poly-disperse GUS-7 particles, which have a mean diameter range between 7-10 μm is the largest (>150%) while the CV for FUS-10, that are mono-disperse, is the smallest (<100%) across all angles.

To investigate the effect of material for larger tracers, we next present μ_p and pdf for GUH-12, PUS-20, FUS-30 and PUS-40 in Figure 9. As noted earlier, the polystyrene particles PUS-20 and 40 have a narrow diameter range. FUS-30 particles have a mean diameter of approximately 30 μm, with a particle diameter range of 10-45 μm. It should be noted that particles chosen for Figure 9 do not have the same diameter. However, with increasing particle diameter, the scattered intensity should increase. Therefore, a significant departure from this trend can be attributed to the effect of material.

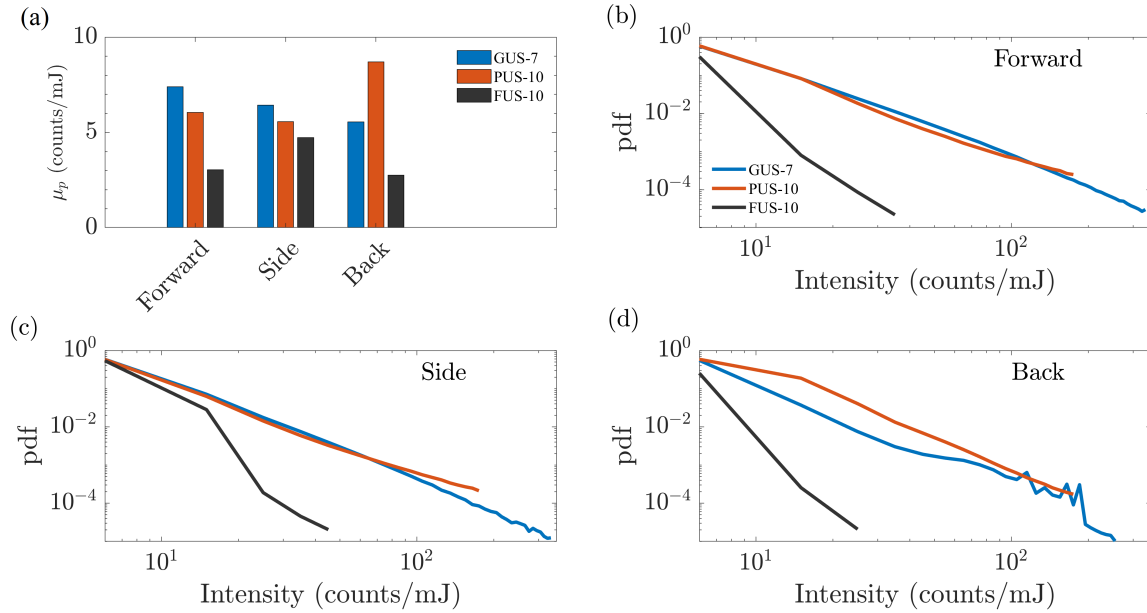From Figure 9a, we can note that between GUH-12 and PUS-20, the glass particles

Figure 8: (a) The normalized mean intensity (μ_p) of GUS-7, PUS-10 and FUS-10 particles for the three viewing angles. The pdf of normalized particle intensity are shown for (b) forward-scatter (c) side-scatter and (d) back-scatter viewing angles.

Figure 9: (a) The normalized mean intensity (μ_p) of GUH-12, PUS-20, FUS-30 and PUS-40 tracers for the three viewing angles. The pdf of normalized particle intensity are shown for (b) forward-scatter (c) side-scatter and (d) back-scatter viewing angles.
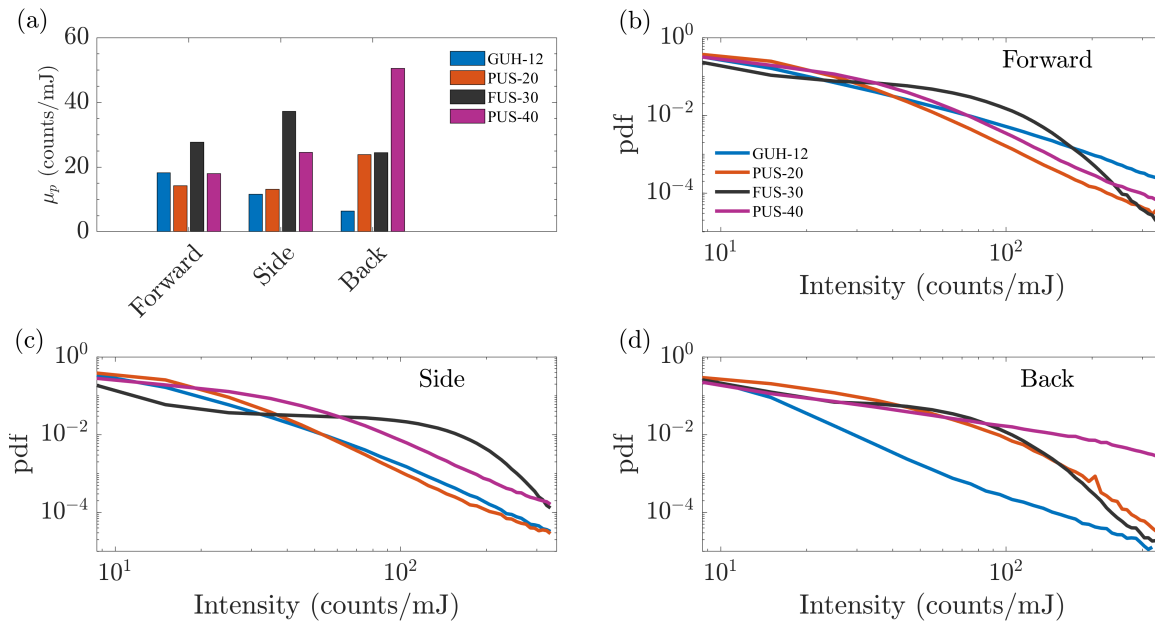
have higher intensity in the forward-scatter, while the polystyrene particles have higher μ_p in back-scatter. This is consistent with the observation based on Figure 8. The side-scatter value of μ_p for PUS-20 is marginally higher than GUH-12. The comparison between the pdf of GUH-12 and PUS-20 in Figure 9b-d shows that in side-scatter the distribution is almost similar. However, in forward-scatter the pdf of GUH-12 is higher than PUS-20 at large intensities. In back-scatter, the pdf of PUS-20 is significantly higher than that of GUH-12.

A comparison between FUS-30 and PUS-40 in Figure 9a shows that the fluorescent particles have higher μ_p in the side-scatter, while the polystyrene particles have significantly higher μ_p in back-scatter. The pdf of FUS-30 and PUS-40 in Figure 9b-d shows that in forward and side-scatter cameras, FUS-30 has a narrower intensity distribution that drops off sharply at about 100 counts/mJ. We also find that the pdf of PUS-40 in back-scatter is significantly higher for larger intensities.

For the fluorescent particles, as noted previously in section 1, the isotropic emission of light due to fluorescence should ideally result in similar intensity for all viewing angles. However, for both FUS-10 and FUS-30, we note higher mean intensity in the side-scatter configuration (1.3 - 1.6×) compared to other viewing angles. This suggests additional side-scatters due to light reflection. The mean intensities in the forward and backward scatter cameras, however, are approximately similar.

From Table 2, we note that the CV of GUH-12 particles is larger than 150%, while the CV of PUS-20 is smaller than 130% for all viewing angles. This is similar to the comparison made between GUS-7 and PUS-10, where the poly-disperse glass particles have a larger CV than the mono-disperse polystyrene particles. A comparison between PUS-40 and FUS-30 shows that the CV for polymer particles is higher in the forward and back-scatter angles relative to the fluorescent particles.

In conclusion, we find that the glass particles result in higher intensities in the forward-scatter direction. The polystyrene particles have a higher back-scatter intensity, while the fluorescent particles have a higher side-scatter intensity. The intensity distribution, as also noted from the CV, is found to be wider for the poly-disperse particles across all viewing angles. The CV for the fluorescent particles is typically lower than the glass and polymer particles suggesting a narrower intensity distribution.

3.3. Effect of heterogeneity

The particle heterogeneity is also an important parameter in determining the light scattering characteristics. This is investigated by comparing the scattered intensity from the five different glass particles in Figure 10. These include glass spheres that are homogeneous (GUS-7), silver-coated (GSS-2), hollow and uncoated (GUH-12), and hollow and silver-coated (GSH-10, GSH-13).
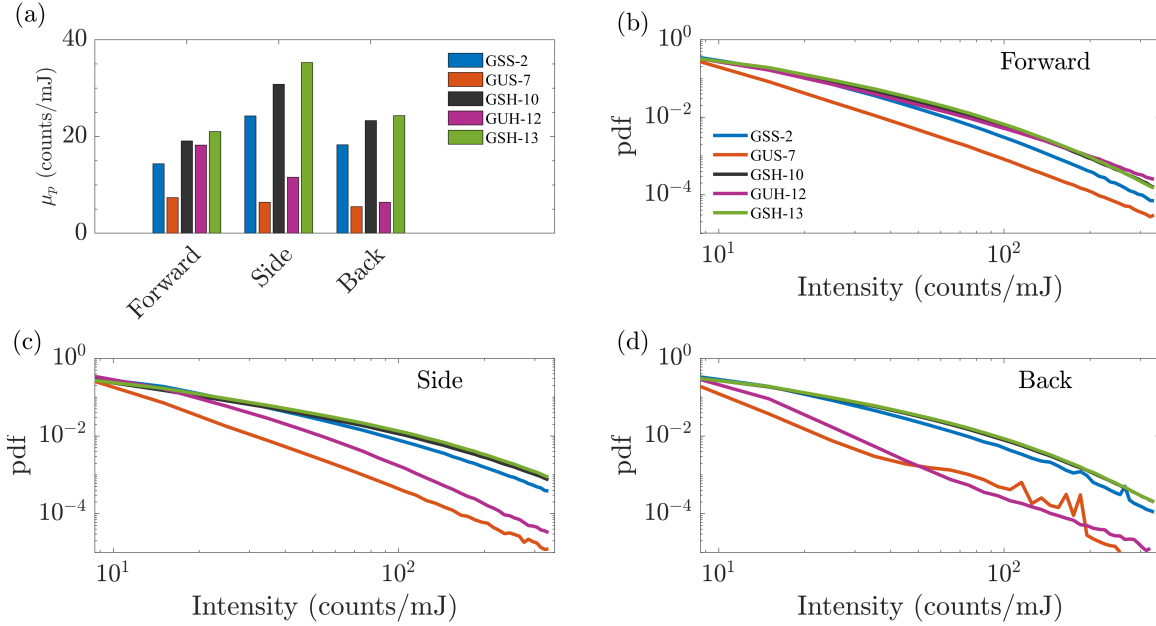

Figure 10: (a) The normalized mean intensity (μ_p) of various glass particles (GSS-2, GUS-7, GSH-10, GUH-12, GSH-13) for the three viewing angles. The pdf of normalized particle intensity are shown for (b) forward-scatter (c) side-scatter and (d) back-scatter viewing angles.

We first note from Figure 10a, that across all viewing angles, silver-coated hollow glass spheres (GSH-10 and GSH-13) have the highest μ_p. We also find that the μ_p of GSH-13 is marginally higher than GSH-10 in all angles, as expected due to the larger particle diameter. Next, we note that the small silver-coated spheres GSS-2 have approximately 2 to 4 times higher μ_p when compared to the larger uncoated GUS-7, across all viewing angles. Similarly, GSH-10 have 2 to 4 times higher μ_p when compared with GUH-12, primarily in side-scatter and back-scatter. This is anticipated, since metallic coating increases reflectivity and is expected to improve side and back-scatter characteristics [13]. It can be noted from Figure 10a and Table 2, that for

all the silver-coated particles (GSS-2, GSH-10, GSH-13), the μ_p of the side-scatter viewing angle is approximately 1.6 times their corresponding forward-scatter values. Also, for silver-coated cases the back-scatter mean intensity is approximately 1.2 times the corresponding forward-scatter mean intensity. We noted previously from the Mie scatter plot in Figure 1, that the forward, back and side-scatter in the case of the silver sphere are expected to be approximately similar, with the forward-scatter being high only in a small region close to $\theta = 0°$. However, it should be noted that the tracers used here are made of glass with a thin silver coating (~ 100 nm). This suggests that the refractive index of coated glass spheres may not necessarily be equal to that of a homogeneous silver sphere. This could possibly be the reason why we find higher side-scatter compared to back-scatter in the silver-coated cases.

The uncoated glass particles, GUS-7 and GUH-12, have lower μ_p in the side and back-scatter directions as seen in Figure 10a. The μ_p of hollow tracers GUH-12 is high in the forward-scatter, and is close to the silver-coated hollow tracers GSH-10 and GSH-13. These observations show that hollow particles have high forward-scatter intensity, and metal coating improves the side-scatter and back-scatter intensities. This is also supported by the observation that GUS-7 particles, which are homogeneous glass particles, have the least μ_p across all viewing angles in comparison.

Figures 10b-d also show that the pdf distribution of scattered intensity is significantly higher for silver-coated tracers in the side and back-scatter directions. In the forward-scatter direction, this difference is smaller between the uncoated hollow tracers and the silver-coated tracers. The scattered intensity of homogeneous particles GUS-7 is typically the lowest in all viewing angles. Table 2 also shows that the CV is approximately between 150 - 160 % across all particles and viewing angles. The only exceptions to these are the uncoated particles GUS-7 and GUH-12 which have a higher CV in the forward-scatter.

3.4. Intensity fluctuations along 3D-PTV tracks

In this section, we investigate the sources that can result in intensity fluctuation along the 3D particle tracks. Figure 11 shows sample tracks of PUS-81 particles obtained using the STB algorithm in Davis 10 (LaVision GmbH). The particles are color-coded with a non-dimensional particle intensity factor, I, computed in Davis 10 based on the iterative particle reconstruction method (IPR) [25]. The intensity factor, I, is evaluated by normalizing the particle intensity with the corresponding OTF intensity. We note

that the value of I varies along individual tracks. Some of the tracks show large intensity intermittency with I varying between 0 to 1.5.

To investigate intensity fluctuations along the 3D trajectory of the particles, we compute the standard deviation (σ_{tr}) and mean (μ_{tr}) of I for every track that is longer than 10 time-steps. The μ_{tr}/σ_{tr} ratio is averaged then across all tracks and is indicated as CV_{tr}. The CV_{tr} percentage for all the particles is shown in the last column of Table 2. The first observation that can be made is that the fluorescent particles have the smallest CV_{tr} of 45-47%. In contrast, the highest CV_{tr} of approximately 70% is noted for the homogeneous glass particles (GUS-7) and the larger silver-coated particles (GSH-13). All the other particles, which include glass and polymer particles of different sizes, have CV_{tr} in the range of approximately 50 - 60 %. In general, CV_{tr} of all the particles is relatively larger, which suggests that the large variation in I along the tracks may not be due to structural asymmetry of the particles. For example, the PUS-10, PUS-20, and PUS-40 particles are perfectly spherical, but they still demonstrate a large variation in I as seen by the CV_{tr} values in the range of 58-62%. The SEM images of Figure 2 indicated that, except GSS-2 and PUS-5, all other particles are spherical and geometrically symmetric.
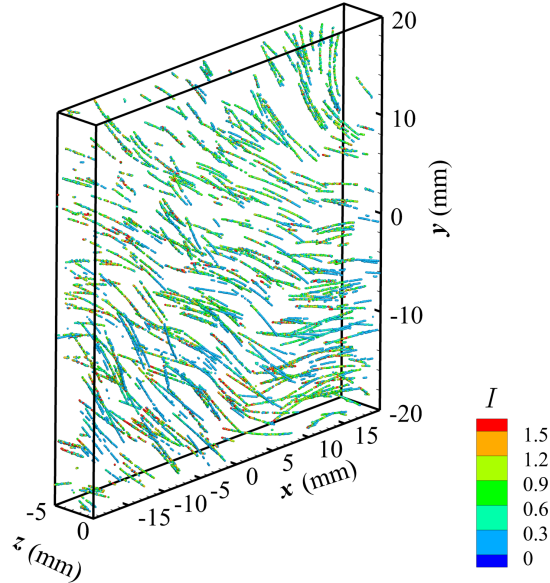

Figure 11: A sample of the 3D tracks obtained using the 'shake-the-box' algorithm for PUS-81 particles. A total of 10 time-steps are shown in the figure to highlight the particle tracks.

In general, factors such as multi-scattering, blockage of the camera line-of-sight,

spatial and temporal variation in laser light energy, and particle image discretization can also result in the observed intensity fluctuations along the 3D tracks. However, the effect of multi-scattering and blockage of the camera line-of-sight by the particles is expected to be negligible in the present experiments due to the small number-density of particles (0.001 ppp, 70 particles/cm^3). The spatial distribution of laser intensity was also estimated using the MART reconstruction in Figure 6. The results showed that the intensity variation was relatively small and limited to 10% of the average light intensity across the measurement volume. The effect of two remaining parameters, namely temporal variations of laser energy and particle image discretization, are discussed below.

To investigate the temporal variation of laser intensity, we averaged the intensity of all particles detected at each time instant. This quantity is indicated by (μ_i), where the subscript i denotes averaging the particle intensity in a single image. This averaging is different from the previously used averaging of particle intensities over the entire data-set, which was shown by subscript p. The average particle intensity for each image can show the fluctuations of the laser power since it cancels out the intensity variations of individual particles. A plot of μ_i versus time for PUS-10, PUS-40, and PUS-81 is presented in Figure 12. Due to the significant size difference, laser energy of 22.2, 11.6 and 1.7 mJ/pulse was used for PUS-10, PUS-40 and PUS-81, respectively. We first note that the μ_i values for PUS-10 and PUS-40 remain approximately constant with time; the peak-to-peak fluctuation being less than 10% of the mean value. In contrast, we note a periodic variation of μ_i, with a peak-to-peak fluctuation of approximately 25% of the temporal mean, for the PUS-81 case that were imaged at a low pulse energy of 1.7 mJ/pulse. This indicates a larger fluctuation of laser power at low power settings, which is common for most lasers. Therefore, a high power setting is recommended to avoid temporal fluctuations of the laser source energy.

To further characterize the fluctuation of the laser power, the ratio of the standard deviation to the mean of μ_i is computed across all the images for each tracer. This parameter is denoted by CV_i and is defined as $\frac{\sigma_{\mu_i}}{\mu_{\mu_i}} \times 100$. For brevity, it is only presented for the side-scatter camera in Table 2. From Table 2, we note that CV_i varies in the range of 1-6 % for all particles. The largest CV_i values are for PUS-10, FUS-30 and PUS-81 tracers. Overall, the small (CV_i) values suggests that the temporal fluctuations in laser energy is small.

The above investigations demonstrated that particle structure, multi-scattering,
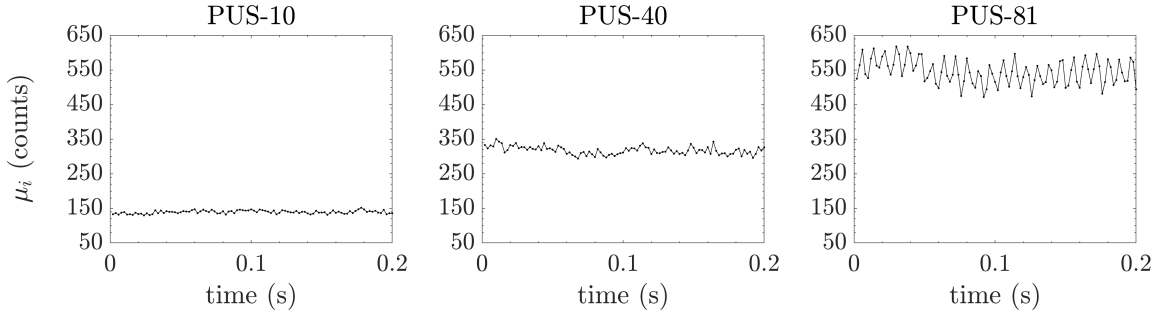
Figure 12: The average particle intensity per image as a function of time. The PUS-10, PUS-20 and PUS-81 tracers are imaged using a laser energy of 22.2, 11.6 and 1.7 mJ/pulse, respectively.
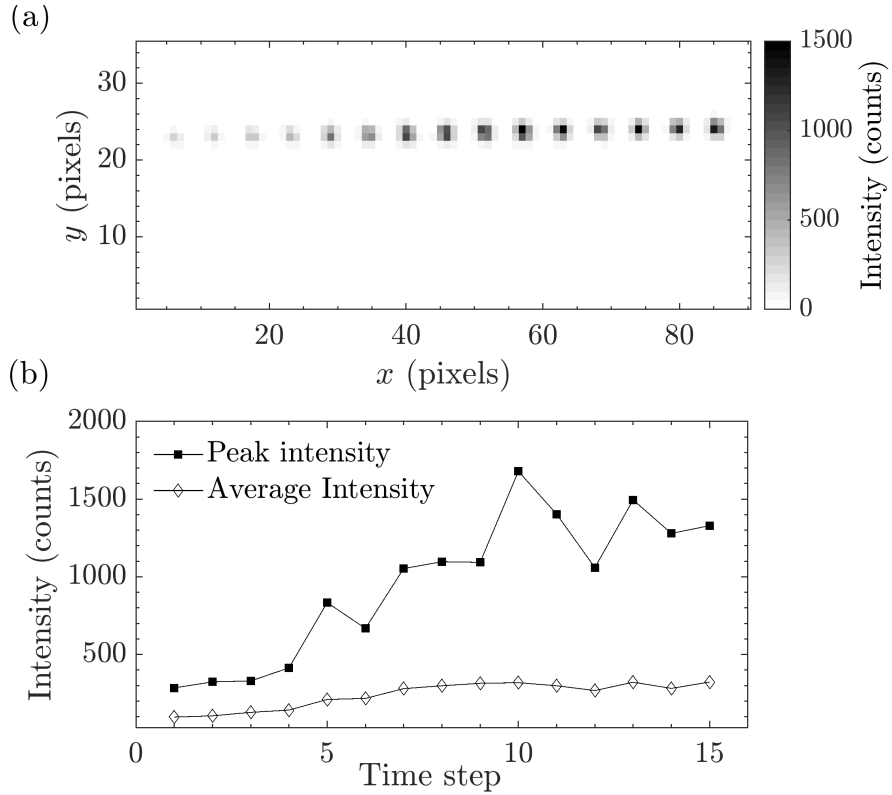

Figure 13: (a) The intensity and location of a single FUS-30 particle over 15 consecutive time-steps. The x location of the particle artificially shifted by 5 pixels over each time-step for clear visualization. (b) The peak and average intensity of the particle for the 15 time-steps. A video of the particle intensity variation in 2D images is also provided in the supplementary material.

blockage of camera line-of-sight, and temporal and spatial variations of laser energy can not be the main cause of the intensity variations along the 3D tracks. This hints to

evaluate discretization of particle images by the pixel array of the CMOS sensor as the remaining factor. Figure 13a shows 2D images of a fluorescent tracer (FUS-30) from 15 successive image frames. In this figure, to avoid overlap of particle images, a 5-pixel shift in the x direction is added to the actual particle displacement between each pair of successive images. The particle image is initially weak and gradually intensifies. As it was discussed in Section 2.2, this is potentially due to the motion of the particle across the edge of the laser sheet. The particle image is approximately 3 pixel in diameter and has a clear intensity peak. However, due to image discretization, the particle images are not symmetric and their intensity peak is not always at the center of the particle image. This issue results in strong fluctuations of the peak intensity as seen in Figure 13b. In contrast, the variation in average particle intensity, also shown in Figure 13b, is relatively small. This sample image suggests that particle image discretization can result in significant variations of the particle peak intensity in the 2D images, and consequently can result in the variations of I in the 3D tracks shown in Figure 11. A detailed characterization of the relation between the 2D particle images and the intensity fluctuations along 3D tracks requires investigating the effect of STB and IPR parameters and is beyond the scope of this study.

4. Conclusion

The present work made a direct comparison between the scattering characteristics of twelve commonly used tracer particles in water. The specific objective of this study was to investigate the effects of size, material, and heterogeneity on the light scattering characteristics of various particles from for forward, side, and back-scatter directions. The image intensity from each imaging direction was then used to make comparisons across particles with different properties. We also performed 3D-PTV experiments using four cameras to investigate the variation of light intensity along 3D particle tracks. A summary of the main observations made is presented below.

(i) The effect of tracer size was studied using mono-disperse polystyrene tracers with a refractive index of 1.59. We found that the peak intensity of the particle image increased approximately linearly with particle diameter. However, the rate of increase in peak intensity with increasing diameter was found to be depend on the viewing angle.

(ii) The results showed that homogeneous glass particles had the largest intensity in

the forward-scatter direction. The polystyrene tracers had the largest intensity in the back-scatter direction, while the fluorescent tracers were brighter in the side-scatter direction. The intensity distribution for most glass tracers was wider than other materials, while the fluorescent particles had a relatively narrow intensity distribution.

(iii) Heterogeneity in tracers was found to increase the scatter intensity. Specifically, silver coating in glass tracers improved the side and back-scatter by 2 - 4 times, when compared with uncoated glass particles. The hollow glass tracers, irrespective of the coating, had higher forward-scatter compared to the homogeneous glass tracers. The non-sphericity of the polyamide particles resulted in a stronger intensity in the forward and side-scatter directions.

(iv) The intensity fluctuation along the 3D particle tracks was large for all the particles and was mainly associated with particle image discretization by the camera sensor. The investigations showed that the effect of structural asymmetry of the particles, and the spatial and temporal variation of laser power was negligible.

References

[1] A Melling. Tracer particles and seeding for particle image velocimetry. *Measurement Science and Technology*, 8(12):1406–1416, 1997.

[2] F Scarano. Tomographic PIV: principles and practice. *Measurement Science and Technology*, 24(1):012001, 2012.

[3] D Schanz, S Gesemann, and A Schröder. Shake-the-box: Lagrangian particle tracking at high particle image densities. *Experiments in Fluids*, 57(5):70, 2016.

[4] S Ghaemi and F Scarano. Multi-pass light amplification for tomographic particle image velocimetry applications. *Measurement Science and Technology*, 21(12), 2010.

[5] A Schröder, R Geisler, G E Elsinga, F Scarano, and U Dierksheide. Investigation of a turbulent spot and a tripped turbulent boundary layer flow using time-resolved tomographic PIV. *Experiments in Fluids*, 44(2):305–316, 2008.

[6] M Raffel, C E Willert, F Scarano, C J Kähler, S T Wereley, and J Kompenhans.

Particle Image Velocimetry: A Practical Guide. Springer International Publishing, 2018.

[7] F Scarano, S Ghaemi, G C A Caridi, J Bosbach, U Dierksheide, and A Sciacchitano. On the use of helium-filled soap bubbles for large-scale tomographic PIV in wind tunnel experiments. *Experiments in Fluids*, 56(2):42, 2015.

[8] J Bosbach, M Kühn, and C Wagner. Large scale particle image velocimetry with helium filled soap bubbles. *Experiments in Fluids*, 46(3):539–547, 2009.

[9] B Gibeau and S Ghaemi. A modular, 3d-printed helium-filled soap bubble generator for large-scale volumetric flow measurements. *Experiments in Fluids*, 59(12):178, 2018.

[10] D Ragni, F Schrijer, B W Van Oudheusden, and F Scarano. Particle tracer response across shocks measured by PIV. *Experiments in Fluids*, 50(1):53–64, 2011.

[11] S Ghaemi, A Schmidt-Ott, and F Scarano. Nanostructured tracers for laser-based diagnostics in high-speed flows. *Measurement Science and Technology*, 21(10):105403, 2010.

[12] R J Adrian and C-S Yao. Pulsed laser technique application to liquid and gaseous flows and the scattering power of seed materials. *Appl. Opt.*, 24(1):44–52, 1985.

[13] R J Adrian and J Westerweel. *Particle Image Velocimetry.* Cambridge University Press, 2011.

[14] C F Bohren and D R Huffman. *Absorption and Scattering of Light by Small Particles.* John Wiley & Sons Ltd., 1998.

[15] H U Yang, J D'Archangel, M L Sundheimer, E Tucker, G D Boreman, and M B Raschke. Optical dielectric function of silver. *Phys. Rev. B*, 91:235137, Jun 2015.

[16] P Laven. *MiePlot v4.6.14*, 2018 (accessed June 4, 2020).

[17] B McKeon et al. Velocity, Vorticity, and Mach number. In : C Tropea, A L Yarin, and J F Foss, editors, *Springer Handbook of Experimental Fluid Mechanics*, pages 215–471. Springer Berlin Heidelberg, 2007.

[18] W Abu Rowin and S Ghaemi. Streamwise and spanwise slip over a superhydrophobic surface. *Journal of Fluid Mechanics*, 870:1127-1157, 2019.

[19] G Sridhar and J Katz. Drag and lift forces on microscopic bubbles entrained by a vortex. *Physics of Fluids*, 7(2):389–399, 1995.

[20] S von Kann, J H Snoeijer, and D van der Meer. Phase diagram of vertically vibrated dense suspensions. *Physics of Fluids*, 26(11):113302, 2014.

[21] P D Cunningham, N N Valdes, F A Vallejo, L M Hayden, B Polishak, X Zhou, J Luo, A K-Y Jen, J C Williams, and R J Twieg. Broadband terahertz characterization of the refractive index and absorption of some important polymeric and organic electro-optic materials. *Journal of Applied Physics*, 109(4):043505–043505–5, 2011.

[22] B Wieneke. Volume self-calibration for 3D particle image velocimetry. *Experiments in Fluids*, 45(4):549–556, 2008.

[23] D Schanz, S Gesemann, A Schröder, B Wieneke, and M Novara. Non-uniform optical transfer functions in particle imaging: calibration and application to tomographic reconstruction. *Measurement Science and Technology*, 24(2):024009, 2012.

[24] G E Elsinga, F Scarano, B Wieneke, and B W van Oudheusden. Tomographic particle image velocimetry. *Experiments in Fluids*, 41(6):933–947, 2006.

[25] B Wieneke. Iterative reconstruction of volumetric particle distribution. *Measurement Science and Technology*, 24(2):024008, 2012.